Annals of Biomedical Engineering
https://doi.org/10.1007/s10439-026-04055-3

BMES BIOMEDICAL ENGINEERING SOCIETY

ORIGINAL ARTICLE

Machine Learning Prediction of Vaginal Tissue Tears Using Finite Element Simulations Informed by Planar Biaxial Testing

Mostafa Zakeri[1] · Justin Krometis[2] · Traian Iliescu[3] · Raffaella De Vita[1]

Received: 11 August 2025 / Accepted: 22 February 2026

Abstract

Purpose Vaginal tissue tearing during childbirth is a prevalent injury with potential long-term consequences, yet the mechanical factors influencing tear behavior remain poorly understood due to the difficulty of conducting in vivo studies. This study aims to investigate how tear geometry and fiber orientation influence local stress and strain patterns, and whether machine learning (ML) can accurately predict tissue responses from finite element (FE) simulation data.

Methods Previously characterized swine vaginal tissue, tested via planar biaxial loading, was used to calibrate the Holzapfel–Gasser–Ogden (HGO) hyperelastic constitutive model. FE simulations were conducted for a range of tear orientations, tear sizes, and fiber alignments to evaluate stress and strain distributions near the tear boundary. Four ML models, linear regression with Stochastic Gradient Descent, Random Forest, Support Vector Regression, and Extreme Gradient Boosting (XGBoost), were trained and evaluated on the FE-generated dataset.

Results The HGO-based FE simulations reproduced experimental results with high fidelity, validating the modeling approach. XGBoost achieved the highest predictive accuracy across all mechanical and geometric outputs. Sensitivity analysis via permutation tests revealed that the initial orientation of the elliptical tear was the most influential predictor of high local stress and strain at the tear during extension.

Conclusion This integrated FE–ML approach enables rapid, accurate prediction of vaginal tissue behavior under varied tear conditions without additional simulations or experimental tests. By leveraging synthetic data, it provides a powerful tool for injury risk evaluation and supports clinical decision-making in maternal health, particularly where in vivo studies are limited.

Keywords Women's health · Vaginal tissue · Vaginal tearing · Finite element methods · Machine learning

Introduction

Childbirth, while a natural process, often results in significant trauma to the vaginal and perineal regions, leading to a range of short- and long-term complications. Vaginal lacerations are particularly common due to the substantial stretching required to accommodate the passage of the baby. Over 80% of women experience some form of laceration during vaginal delivery, with first-time mothers at especially high risk [1]. Risk factors that increase the likelihood of such tears include birth weight, prolonged labor, and instrumental deliveries, such as forceps, vacuum extraction, and episiotomy [1–3]. While childbirth is the most common cause, vaginal lacerations may also result from other causes like sexual intercourse [4] or traumatic injury [5]. Given the vagina's essential role in pelvic floor support [6], such tears can significantly compromise pelvic health. Despite recognizing these risk factors, most evidence remains observational and

Associate Editor Estefanía Peña oversaw review of this article.

✉ Raffaella De Vita
devita@vt.edu

Mostafa Zakeri
zakeri@vt.edu

Justin Krometis
jkrometi@vt.edu

Traian Iliescu
iliescu@vt.edu

[1] Department of Mechanical Engineering, Virginia Tech, 325 Stanger Street, Blacksburg, VA 24061, USA

[2] National Security Institute, Virginia Tech, 1311 Research Center Drive, Blacksburg, VA 24061, USA

[3] Department of Mathematics, Virginia Tech, 225 Stanger Street, Blacksburg, VA 24061, USA

Published online: 12 March 2026

heavily reliant on clinical experience, underscoring the need for a novel, data-driven approach grounded in a comprehensive dataset to improve accuracy and support real-time decision-making. Such an approach would help physicians prevent and minimize tears more effectively and enhance treatment outcomes.

The mechanical response of vaginal tissue has been investigated using different experimental techniques [7]. Uniaxial tensile testing has been widely employed [8, 9], while fewer studies have implemented planar biaxial testing to better capture the tissue's anisotropic mechanical behavior [10–13]. These approaches have significantly advanced the characterization of vaginal tissue mechanics but are often limited by measurement variability, high costs, and labor-intensive protocols. To address these challenges, finite element (FE) modeling has emerged as a powerful alternative, as it allows for more controlled, comprehensive, and efficient analyses.

FE models have been widely used to investigate how the female pelvic floor responds to significant physiological loads, such as those experienced during childbirth, as well as to chronic or surgical alterations in support structures (e.g., prolapse) [14–16]. Early efforts primarily focused on the levator ani: some groups simulated its stretching, contraction, and load-bearing role during vaginal delivery [17, 18], while others mapped the resulting intramuscular stress fields [19]. Over time, investigators expanded FE analyses to additional pelvic floor components, including the uterosacral ligaments [20] and superficial perineal muscles [21], to better understand how these structures share or redistribute load. In most studies, the vaginal canal is analyzed within a whole-pelvis FE model. Only a handful of investigations have examined it in isolation, either for device-safety testing [22] or for reduced-order modeling development [23–25]. In our previous work, based on experimental inflation tests of rat vaginal tissue, we employed FE modeling (in combination with reduced-order modeling approaches) to examine tissue response [23], the influence of tear presence [24], and the subsequent progression of tears [25]. Despite these advances, opportunities remain to further investigate vaginal tissue mechanics through FE modeling, particularly with regard to the behavior of tissue tears. Although FE modeling offers an effective means of exploring scenarios that may be difficult, costly, or impossible to replicate experimentally, especially in vivo, it also poses challenges such as complex model formulation, high computational demands, and the need for accurate geometries, boundary conditions, and material properties [14, 26].

Fast and accurate predictions are often critical in obstetric care, where timely decisions can affect maternal outcomes and prevent injury. Machine learning (ML) offers a promising solution by enabling real-time, data-driven predictions based on *prior* patient information, significantly accelerating FE method-based simulations [27, 28]. In the context of reproductive health and vaginal tissue, ML has been applied to various prediction tasks primarily related to clinical risk analysis. For instance, it has been used to estimate the risk of postpartum hemorrhage following vaginal delivery, with gestational age and maternal weight identified as the most significant predictors [29]; to forecast preterm birth using cervical length, vaginal microbiota profiles, and white blood cell counts [30]; and to predict individualized success probabilities of vaginal birth after cesarean delivery based on several maternal features, fetal features, and previous obstetric outcomes [31].

ML approaches are promising for supporting timely clinical decisions in pregnancy, such as whether to proceed with vaginal delivery or perform a cesarean section, but developing reliable models requires extensive training datasets that are difficult to obtain through in vivo or ex vivo experiments due to ethical, logistical, and technical constraints. FE simulations become essential, providing synthetic datasets that complement experimental studies and can be used to develop and validate predictive ML algorithms. Ultimately, integrating FE and ML methods offers a robust and efficient framework for real-time prediction of vaginal tissue deformations under physiological loading, with direct relevance to scenarios such as childbirth planning and maternal trauma prevention. Recently, hybrid approaches have been applied to simulate pelvic floor muscle deformations during vaginal delivery [32, 33], while we have employed similar methods to model vaginal tissue deformation under inflation loading [23], as well as to investigate the effects of tears [24] and their propagation under such loading conditions [25].

This study aims to predict the mechanical behavior of vaginal tissue containing a tear by combining experimental data, FE modeling, and ML techniques. To achieve this, we utilized previously published experimental data, obtained from planar biaxial testing of swine vaginal tissue with pre-imposed tears oriented along the longitudinal (LD) and circumferential (CD) directions [10]. These data were used to identify the material parameters for the Holzapfel–Gasser–Ogden (HGO) constitutive model implemented in our FE simulations. Following calibration, we conducted simulations to examine the influence of geometric factors, including initial tear orientation and size, on the mechanical response of vaginal tissue. We also evaluated the impact of the mean preferred fiber orientation, which is used to introduce anisotropy in the HGO model, on tissue behavior. Building on these simulations, we trained multiple ML models using four distinct algorithms, i.e., linear regression with stochastic gradient descent (SGD), random forest (RF), support vector regression (SVR) with a nonlinear kernel, and extreme gradient boosting (XGBoost) to predict mechanical outputs such as local stress and strain near the tear, as well as geometric characteristics like tear size during loading.

The performance of the trained models was evaluated by predictive accuracy, with training time also recorded for reference. A permutation test was then applied to the most accurate model to identify the input parameters with the greatest influence on the predictions. This novel integrated FE–ML approach advances our understanding of vaginal tissue mechanics by analyzing how variations in tear orientation, tear size, and tissue anisotropy alter local stress and strain fields. Our findings have the potential to improve early identification of tear risk, inform strategies to prevent tear propagation, and support the development of more effective treatments for vaginal injuries.

Methods

FE Models

This section describes the FE models developed to simulate the experimentally measured tear behavior of swine vaginal tissue under planar biaxial testing [34]. First, the model geometry and boundary conditions are presented, followed by the use of the HGO model to characterize the anisotropic hyperelastic properties of vaginal tissue. Next, we compare the FE simulation results with experimental data to assess overall agreement. Finally, we present the effect of changing the tear and tissue characteristics, such as tear orientation, tear size, and mean preferred fiber orientation, on the mechanical response of vaginal tissue around the tear. All FE simulations were conducted using Abaqus/Standard (Abaqus 2020, Dassault Systèmes Americas Corp., Waltham, MA) on a workstation with a 28-core Intel® Xeon® Gold 6258R CPU operating at 2.70 GHz, with 191 GB of RAM, and supported by an NVIDIA® Quadro RTX 4000™ GPU with 8 GB of RAM and 2304 CUDA® cores.

Geometries and Boundary Conditions

In this study, we developed FE models informed by experimental data from McGuire et al. [10], who examined the mechanical behavior of vaginal tissue specimens under biaxial tension. Specifically, McGuire et al. [10] conducted planar equi-biaxial tests on square vaginal tissue specimens, with specimen edges aligned to the LD and CD of the vagina, using swine as an animal model. Swine was selected as the animal model because its vaginal tissue exhibits anatomical and morphological characteristics similar to those of humans, as confirmed by histological analyses [35]. Testing was performed on specimens with (a) no tear (NT), (b) a pre-imposed elliptical longitudinal tear (LT), (i.e., the major axis of the tear aligned with the LD), and (c) a pre-imposed elliptical circumferential tear (CT, i.e., the major axis of the tear aligned with the CD). Directional stretch ratios along the LD and CD were measured for the NT specimens using the digital image correlation method, while axial displacements of hooks holding the specimens were recorded for all specimens in both the LD and CD. Since the presence of tears in the LT and CT groups prevented strain measurements, the normalized hook displacement (NHD), defined as the ratio of the average hook distance in the deformed configuration to the average hook distance in the undeformed configuration in the LD or CD, was used as a measure of the tissue's stretch instead. In each direction, the axial nominal stress was calculated by dividing the total reaction force applied to the four hooks by the corresponding cross-sectional area, determined as the product of the distance between the two outermost hooks and the tissue thickness. Hereafter, we refer to this quantity simply as "stress."

Ten distinct vaginal tissue geometries were analyzed: one geometry with no tear; five geometries with a centrally placed elliptical tear of fixed size oriented at different angles; and four additional geometries with centrally placed elliptical tears of varying sizes, all oriented along the LD. The baseline geometry with a pre-imposed LT is shown in Fig. 1a, while the boundary conditions are illustrated in Fig. 1b. The geometry, specimen dimensions, and boundary conditions follow those reported in McGuire et al. [10] (see Table 1 therein for specimen dimensions).

Due to the symmetry of the geometry in the three directions (x-, y-, and z-axes in Fig. 1a), only one-eighth of the domain was modeled to reduce computational costs. For all simulations, the displacement and symmetry boundary conditions along the z-axis were maintained consistently. However, symmetry boundary conditions along the LD (x-axis) and CD (y-axis) were applied only when the tear orientation aligned with these axes. In simulations with tear orientations not aligned with the LD or CD, symmetry along these axes

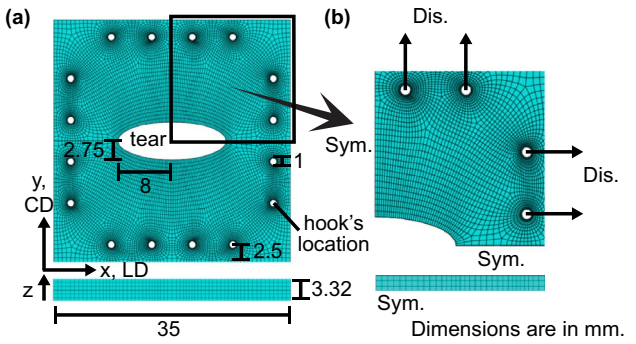

Fig. 1 **a** Top and side views of the baseline LT geometry with dimensions. **b** Boundary conditions applied to one-eighth of the geometry: prescribed displacements (Dis.) at the hook locations; traction-free conditions on the tear surfaces and the external top surface; and symmetry boundary conditions (Sym.) imposed on planes of symmetry introduced by domain reduction

Table 1 Initial values of the semi-minor and semi-major axes of the elliptical tear in the FE model of vaginal tissue specimens

Case	a_0 (mm)	b_0 (mm)
Baseline values	8.0	2.75
Smaller a_0	7.0	2.75
Larger a_0	9.0	2.75
Smaller b_0	8.0	2.25
Larger b_0	8.0	3.25

was not assumed. A displacement boundary condition of 7.5% of the initial distance between the hooks on opposite sides of the specimen was applied uniformly in both directions, resulting in a 15% increase of this distance, or NHD = 1.15. Given the square geometry, this displacement was introduced symmetrically and gradually using a ramp function from the start to the end of the simulation. When a pre-imposed tear was present, no specific boundary condition was applied along the tear boundaries; instead, these boundaries were treated as free (open) with a zero-stress-gradient field.

The finite element mesh consisted of C3D8 elements, i.e., 8-node linear brick elements with full integration. This element formulation was selected for its robust and stable performance in simulations of hyperelastic materials undergoing large deformations, where accurate stress and strain predictions are required. Concerning grid independence, we performed simulations using the LT geometry with four different grid sizes: coarse (884 elements), medium (1300 elements), fine (1850 elements), and finer (2690 elements). The fine grid with 1850 elements for one-eighth of the geometry (3 elements through thickness, accounting for symmetry) represented a reasonable trade-off between accuracy and computational cost and was selected as the reference grid for generating other grids with the same mesh properties to maintain consistency across all simulations.

Constitutive Model and Parameter Calibration

To model the hyperelastic and anisotropic behavior of vaginal tissue, we employed the HGO constitutive model [36], as done in our previous studies [23–25]. The strain energy density function, W, for this model is defined as follows:

$$W = \frac{c}{2}\left(\bar{I}_1 - 3\right) + \frac{1}{D}\left[\frac{J^2-1}{2} - \ln J\right] + \frac{k_1}{2k_2}\sum_{\alpha=1}^{N}\left\{e^{k_2\langle \bar{E}_\alpha\rangle^2} - 1\right\}, \tag{1}$$

where the parameter c corresponds to the shear modulus, the parameter k_1 is a stress-like parameter, and the parameter k_2 is dimensionless. The parameter $D = \frac{2}{K}$, where K is the bulk modulus, defines material compressibility. Moreover, $\bar{I}_1 = \mathrm{tr}(\bar{\boldsymbol{C}})$ represents the first invariant of the deviatoric right Cauchy–Green strain tensor, $\bar{\boldsymbol{C}} = J^{-\frac{2}{3}}\boldsymbol{C}$, where $J = \det(\boldsymbol{F})$, $\boldsymbol{C} = \boldsymbol{F}^{\mathrm{T}}\boldsymbol{F}$ is the right Cauchy–Green strain tensor, and $\boldsymbol{F}$ is the deformation gradient. The strain-like quantity $\bar{E}_\alpha$ in Eq. (1) is defined as follows:

$$\bar{E}_\alpha = \kappa\left(\bar{I}_1 - 3\right) + (1 - 3\kappa)\left(\bar{I}_{4(\alpha\alpha)} - 1\right), \tag{2}$$

where $\bar{I}_{4(\alpha\alpha)} = \boldsymbol{a}_\alpha \cdot \bar{\boldsymbol{C}} \cdot \boldsymbol{a}_\alpha$ represents the fourth invariant of the deviatoric strain for $\alpha = 1, \ldots, n$, with n being the total number of fiber families considered in the model. This invariant characterizes deformation in the direction of the mean preferred fiber orientations defined by the vectors $\boldsymbol{a}_\alpha$. The parameter κ in Eq. (2), where $0 \le \kappa \le \frac{1}{3}$, controls the degree of fiber dispersion within each fiber family. Specifically, when $\kappa = 0$, fibers are perfectly aligned along the preferred direction $\boldsymbol{a}_\alpha$, while $\kappa = \frac{1}{3}$ indicates randomly oriented fibers. The operator $\langle\cdot\rangle$ in Eq. (1) denotes the Macaulay brackets.

The material parameters in the HGO model were identified by iteratively adjusting them in simulations to qualitatively match the average stress versus NHD response observed experimentally for the NT, LT, and CT specimens [10]. Specifically, a single fiber family ($\alpha = 1$) was modeled with the preferred direction defined as $\boldsymbol{a}_1 = (0, \cos\beta, \sin\beta)$, where β is the angle relative to the LD (x-axis in Fig. 1a). In these simulations, we assumed $\beta = 0$ due to the lack of experimental data on the mean preferred fiber orientation in swine vaginal tissue. To calibrate the HGO model, we aimed to preserve consistency in material properties across configurations by fixing $c = 10$ kPa, $D = 6.7$ kPa, and $k_2 = 1$. However, slight adjustments to the fiber-related parameters k_1 and κ were required to best match the experimental data.

Tear Size, Tear Orientation, and Mean Preferred Fiber Orientation

Comparative FE simulations were conducted to determine the effects of tear orientation and size. Consistent with common experimental practice, material parameters identified from intact (NT) specimens were used in all comparative simulations, as the presence of a tear introduces geometric discontinuities and local heterogeneities that confound constitutive parameter estimation. In these simulations, the HGO material parameters were fixed based on calibration with average stress–NHD data from NT specimens ($c = 10$ kPa, $D = 6.7$ kPa, $k_1 = 1400$ kPa, $k_2 = 1$, $\alpha = 1$, $\beta = 0°$, and $\kappa = 0.30$). These parameter values will be referred to as the baseline material parameters.

Tear orientation was examined using five FE geometries, each with an elliptical tear of fixed size defined by initial semi-major and semi-minor axes $a_0 = 8.0$ mm and $b_0 = 2.75$ mm, respectively. This size will be referred to as the baseline

tear size (Table 1). The angle θ between the semi-major axis and the LD was varied across 0°, 22.5°, 45°, 67.5°, and 90°, where $\theta = 0°$ and $\theta = 90°$ correspond to LT and CT, respectively.

The influence of tear size on the mechanical response of vaginal tissue under biaxial extension was investigated by performing four additional FE simulations using geometries with elliptical tears of varying sizes. LT geometries were selected, as most vaginal tears occur along the LD [37]. In addition to the baseline tear size considered above (i.e., $\theta = 0°$), tear sizes were chosen to span the range reported by McGuire et al. [10]. Table 1 lists the selected a_0 and b_0 values prior to applying displacements in the LD (x-axis) and CD (y-axis).

Finally, three additional FE simulations using the LT geometry were carried out to explore how variations in mean preferred fiber orientation influence the mechanical response of vaginal tissue. The tear size was fixed to its baseline value. Two fiber families, that are $\alpha = 2$ in Eqs. (1)–(2), were considered in these simulations. The preferred fiber directions for these two fiber families were defined by the unit vectors $\boldsymbol{a}_1 = (0, \cos\beta, \sin\beta)$ and $\boldsymbol{a}_2 = (0, \cos\beta, -\sin\beta)$ to ensure symmetry about the LD. In addition to the case with $\beta = 0°$ (which is equivalent to having one fiber family) considered above (i.e., $\theta = 0$), three simulations were run for $\beta = 15°$, 30°, and 45°. Each family was assigned a stiffness parameter of $k_1 = 700$ kPa, which was half the value used for simulations with a single fiber family, while all other parameters remained unchanged from the baseline values. This parameter selection preserves the same total fiber contribution as in the single fiber family case and isolates the effect of fiber architecture without changing overall stiffness.

From all twelve simulations, together with the stresses at the hooks and the displacement fields, we extracted the tear semi-major axis a, semi-minor axis b, tear area $A = \pi ab$, maximum (max) von Mises stress (VMS), and max principal strain (MPS) at the tear boundary at each NHD. Although the time increments were determined adaptively by Abaqus during the nonlinear simulations, results were sampled at 61 equally spaced displacement levels between NHD = 1.00 and 1.15 (increments of 0.0025) to adequately resolve the nonlinear mechanical response and ensure consistent data representation for subsequent ML analysis.

ML Model Implementation

In this section, we present the implementation of four ML models, SGD, SVR, RF, and XGBoost, to predict outcomes from FE simulations. Each model was trained using six input features: NHD, tear orientation θ, mean preferred fiber orientation β, initial semi-major axis a_0, initial semi-minor axis b_0, and initial tear area $A_0 = \pi a_0 b_0$. The specific values used for these input features are listed in Table 2. Here, we describe the data preprocessing procedures, model training methodology, and evaluation metrics used to test the predictive performance of the four ML algorithms. As mentioned earlier, 12 simulations were performed, and for each simulation, results were extracted at 61 equally spaced NHD values from 1.00 to 1.15, with 0.0025 increments. This resulted in 732 total samples (12 simulations × 61 NHDs), each represented by a 6-dimensional input vector used to train and evaluate the ML models.

Each input row vector was defined as

$$\boldsymbol{x}_i = (\text{NHD},\ \theta,\ \beta,\ a_0,\ b_0,\ A_0), \tag{3}$$

where $i = 1, \ldots, 732$ indexes the total number of input combinations. The 732 input combinations result from four groups, each defined by the specific parameter variations applied and the NHD value. In the baseline group ($\boldsymbol{x}_1$ to $\boldsymbol{x}_{61}$), all parameters were fixed except NHD: $\theta = 0°$, $\beta = 0°$, $a_0 = 8.0$ mm, $b_0 = 2.75$ mm, and $A_0 = 69.1$ mm^2. The tear orientation group ($\boldsymbol{x}_{62}$ to $\boldsymbol{x}_{305}$) included variations in $\theta \in \{22.5°,\ 45°,\ 67.5°,\ 90°\}$ and NHD values, while the other parameters remained fixed to the baseline values. This resulted in $4 \times 61 = 244$ input combinations. The fiber orientation group ($\boldsymbol{x}_{306}$ to $\boldsymbol{x}_{488}$) varied $\beta \in \{15°,\ 30°,\ 45°\}$ and NHD values, with $\theta = 0°$, $a_0 = 8.0$ mm, and $b_0 = 2.75$ mm, leading to $3 \times 61 = 183$ input combinations. Finally, the tear size group ($\boldsymbol{x}_{489}$ to $\boldsymbol{x}_{732}$) involved varying either $a_0 \in \{7.0,\ 8.0,\ 9.0\}$ mm while fixing $b_0 = 2.75$ mm, or $b_0 \in \{2.25,\ 2.75,\ 3.25\}$ mm while fixing $a_0 = 8.0$ mm, with

Table 2 Input variables and their values used in ML models

Input variable	Values
Normalized hook displacement (NHD)	1.0000, 1.0025,…,1.1500 (61 Values)
Tear orientation (θ)	0°, 22.5°, 45°, 67.5°, 90°
Mean preferred fiber direction (β)	0°, 15°, 30°, 45°
Initial tear size (a_0, b_0, $A_0 = \pi a_0 b_0$)	(7 mm, 2.75 mm, 60.5 mm^2)
	(8 mm, 2.75 mm, 69.1 mm^2)
	(9 mm, 2.75 mm, 77.75 mm^2)
	(8 mm, 2.25 mm, 56.6 mm^2)
	(8 mm, 3.25 mm, 81.7 mm^2)

both $\theta = 0°$ and $\beta = 0°$ held constant and NHD values. These variations produced $5 \times 61 = 305$ input combinations.

Using each ML algorithm, we mapped the input vectors $\boldsymbol{x}_i$, for $i = 1, \ldots, 732$, to five scalar target variables obtained from the FE simulations: deformed semi-major axis a, deformed semi-minor axis, b, deformed tear area A, max MPS, and max VMS. Each ML model was trained to predict a specific output using the same set of input features. Accordingly, each model produced a scalar prediction $\hat{y}_i$ corresponding to the input vector $\boldsymbol{x}_i$, where

$$\hat{y}_i \in \left\{\hat{a}_i,\ \hat{b}_i,\ \hat{A}_i,\ \widehat{\max}(\text{MPS})_i,\ \widehat{\max}(\text{VMS})_i\right\}, \tag{4}$$

with $\hat{a}_i$ and $\hat{b}_i$ denoting the predicted deformed tear semi-major and semi-minor axes, respectively, $\hat{A}_i$ the predicted deformed tear area, and $\widehat{\max}(\text{MPS})_i$ and $\widehat{\max}(\text{VMS})_i$ the predicted max MPS and max VMS, respectively.

ML Models and Training Methodology

Before training any ML models, we first shuffled the dataset and partitioned it into training and testing sets, using 80% of the data for training and the remaining 20% for testing. To ensure numerical stability and fair treatment of all features, we standardized the input variables based on the statistics of the training set, scaling them to have zero mean and unit variance. This preprocessing step prevented features with larger numerical ranges from dominating the learning process and improved the efficiency and convergence behavior of many learning algorithms. For model evaluation, we used a different loss function for each model but used common criteria for comparing the models' performance.

First, we selected a linear regression model trained with the SGD algorithm due to its simplicity, scalability, and suitability for large datasets [38]. In regression tasks, SGD learns the relationship between the input features $\boldsymbol{x}_i$ and the corresponding FE output scalar y_i by iteratively minimizing a loss function that quantifies prediction error. Unlike traditional (batch) gradient descent, which computes gradients over the entire training set, SGD estimates the gradient using a single data point $(\boldsymbol{x}_i, y_i)$ at each iteration. This makes it particularly efficient and memory-friendly for large-scale problems. In our implementation, the prediction is defined by a linear function of the form:

$$\hat{y}(\boldsymbol{x}) = \boldsymbol{w}\boldsymbol{x}^{\top} + b, \tag{5}$$

where $\boldsymbol{w} \in \mathbb{R}^6$ is the weight row vector mapping input features to outputs, and $b \in \mathbb{R}$ is the bias scalar. Among the input features, geometric parameters such as the semi-major axis, semi-minor axis, and tear area are inherently correlated. To manage potential multicollinearity, we applied ℓ_1 regularization during training to encourage sparsity in the learned weights and allow the model to automatically select the most informative features. We minimized the objective function, J, defined as follows:

$$J(\boldsymbol{w}, b) = \frac{1}{N}\sum_{i=1}^{N} L_\delta(\hat{y}_i, y_i) + \alpha\|\boldsymbol{w}\|_1, \tag{6}$$

where α is the regularization strength, N is the total number of training samples, and L_δ is the Huber loss function. This function is given by

$$L_\delta(y, \hat{y}) = \begin{cases} \frac{1}{2}(y - \hat{y})^2 & \text{if } |y - \hat{y}| \le \delta, \\ \delta\left(|y - \hat{y}| - \frac{1}{2}\delta\right) & \text{otherwise,} \end{cases} \tag{7}$$

where δ is a threshold that determines the point at which the loss transitions from quadratic to linear behavior. The Huber loss function was selected to increase robustness against outliers.

At each iteration t, the parameters are updated as follows:

$$\boldsymbol{w}^{(t+1)} = \boldsymbol{w}^{(t)} - \eta\left[\nabla_{\boldsymbol{w}} L_\delta(\hat{y}_i, y_i) - \alpha\,\text{sign}(\boldsymbol{w}^{(t)})\right], \tag{8}$$

$$b^{(t+1)} = b^{(t)} - \eta\,\nabla_b L_\delta(\hat{y}_i, y_i), \tag{9}$$

where η is the learning rate, which determines the size of each update step. We employed an adaptive learning rate strategy, which adjusted η dynamically based on the gradient history. This helps avoid overshooting minima and improves convergence speed.

We next selected the RF regression algorithm for its effectiveness in modeling nonlinear relationships and its robustness against overfitting. RF is an ensemble method that builds multiple decision trees, each trained on a randomly sampled subset of the training data, a technique known as "bagging" [39]. This process reduces variance and improves generalization by averaging over diverse models. At each node of a tree, a random subset of input features is considered, and the best split is chosen based on an impurity measure. Here, we used the mean absolute error (MAE) as the splitting criterion, defined as follows:

$$\text{MAE} = \frac{1}{N}\sum_{i=1}^{N} |y_i - \hat{y}_i|, \tag{10}$$

where N is the number of samples at a given node. For regression tasks, RF predicts outputs by averaging the predictions of individual trees. Then the final model prediction is given by [40]

$$\hat{y}(\boldsymbol{x}) = \frac{1}{K}\sum_{k=1}^{K} \hat{y}_k(\boldsymbol{x}), \tag{11}$$

where K is the total number of decision trees in the forest, and $\hat{y}_k(\boldsymbol{x})$ represents the prediction made by the kth tree for input $\boldsymbol{x}$. In this study, we set $K = 30$ trees, limited each tree's maximum depth to 7, and used a feature subsampling rate of 0.5 (i.e., only 50% of the features considered at each split) to reduce inter-tree correlation, particularly given the presence of collinear inputs such as the semi-major axis, semi-minor axis, and their derived area.

We then considered the SVR algorithm for its ability to model complex relationships and its robustness in high-dimensional feature spaces [41]. In regression tasks, SVR seeks to model the relationship between the input variables and the predicted response, while allowing small deviations within a predefined tolerance margin, denoted by $\epsilon > 0$. This ϵ-insensitive loss function enables the model to ignore minor errors and penalize only larger deviations, making it well suited for noisy data and reducing sensitivity to outliers. It is defined as

$$L_\epsilon(y, \hat{y}) = \begin{cases} 0 & \text{if } |y - \hat{y}| \le \varepsilon, \\ |y - \hat{y}| - \varepsilon & \text{otherwise.} \end{cases} \tag{12}$$

SVR relies only on a subset of the training data known as "support vectors." These are the training points where the prediction error is greater than ϵ, meaning they fall outside the tolerated margin. Only support vectors contribute to the final model; all other points have a weight of zero and do not affect the learned function.

To capture nonlinear relationships, SVR maps the data into a higher-dimensional feature space using kernel functions. We used the following regression function to make predictions with our SVR model:

$$\hat{y}(\boldsymbol{x}) = \sum_{i=1}^{N} v_i \cdot k(\boldsymbol{x}_i, \boldsymbol{x}) + b. \tag{13}$$

Here, v_i are the weights, b is the bias term, and $k(\boldsymbol{x}_i, \boldsymbol{x})$ is the kernel function that measures the similarity between the input $\boldsymbol{x}$ and training data $\boldsymbol{x}_i$. In this formulation, only the inputs $\boldsymbol{x}_i$ with nonzero v_i are support vectors. These data points lie outside the ϵ margin and are the only ones that influence the final prediction function.

We used the radial basis function (RBF) kernel, a widely adopted choice for nonlinear regression tasks due to its flexibility and smoothness [42]. This kernel is defined as follows:

$$k(\boldsymbol{x}_i, \boldsymbol{x}_j) = \exp\left(-\frac{\|\boldsymbol{x}_i - \boldsymbol{x}_j\|^2}{2\sigma^2}\right), \tag{14}$$

where $\boldsymbol{x}_i$ and $\boldsymbol{x}_j$ are two input vectors, and σ controls the kernel width, affecting how much influence each support vector has, with smaller σ values creating more localized effects and larger values producing smoother, broader generalization. In an RBF kernel, correlated inputs simply result in similar transformed coordinates, and the support vector machinery naturally weights or discards redundant dimensions via the learned v_i. Our SVR implementation used a regularization parameter equal to 1 to control the trade-off between margin size and training error, and $\epsilon = 0.1$.

Lastly, we used the XGBoost method since it can handle large and complex regression tasks and has built-in regularization techniques that prevent overfitting [43]. Unlike RF, which builds trees independently, XGBoost constructs trees sequentially, with each new tree correcting the residuals of the previous ones in a boosting framework. Given the input vector $\boldsymbol{x}$, the prediction of the XGBoost model is obtained by summing the outputs of K regression trees:

$$\hat{y}(\boldsymbol{x}) = \sum_{k=1}^{K} \hat{y}_k(\boldsymbol{x}), \quad \hat{y}_k \in \mathcal{F}, \tag{15}$$

where $\hat{y}_k(\boldsymbol{x})$ represents the prediction of the kth tree and $\mathcal{F}$ denotes the space of all possible regression trees.

At each boosting round t, a new tree $f_t(\boldsymbol{x})$ is selected to minimize the regularized objective function [43]:

$$f_t = \arg\min_{f \in \mathcal{F}} \left[\sum_{i=1}^{N} L(y_i, \hat{y}_i^{(t-1)} + f(\boldsymbol{x}_i)) + \Omega(f) \right], \tag{16}$$

where L is the loss function measuring prediction error, and $\Omega(f)$ is a regularization term that penalizes model complexity by combining the number of leaves in the tree, with ℓ_1 and ℓ_2 penalties on the leaf weights, thereby reducing overfitting. Once f_t is found, the prediction for each sample is updated by adding the new tree's output to the previous prediction:

$$\hat{y}_i^{(t)} = \hat{y}_i^{(t-1)} + \eta f_t(\boldsymbol{x}_i), \tag{17}$$

where η is the learning rate that controls the step size of the update. The loss function considered here is mean squared error (MSE), defined as follows:

$$\text{MSE} = \frac{1}{N} \sum_{i=1}^{N} (y_i - \hat{y}_i)^2, \tag{18}$$

where N is the number of samples at a given node. In this study, we used the GBTree booster, which constructs trees using a greedy, depth-first strategy by minimizing the loss function at each split. We set the number of estimators to 1500, the maximum tree depth to 70, the learning rate to 0.01, and both ℓ_1 ($\alpha = 0.5$) and ℓ_2 ($\lambda = 0.5$) regularization parameters to moderate values. These hyperparameters were tuned to balance model accuracy and complexity, ensuring good generalization performance.

We trained a total of 20 models, one for each combination of 4 ML algorithms (linear regression with SGD, RF,

SVR, and XGBoost) and 5 output variables as illustrated in Fig. 2a. For each model, fivefold cross-validation was used during training to enhance generalization and reduce overfitting. An example is shown in Fig. 2b, where five separate linear models with SGD were trained to predict a, and their predictions were averaged to generate the final output.

Hyperparameters were optimized via grid search for each model. Any model hyperparameters not explicitly reported were either set to default values or had minimal impact on performance when tuned. All training and evaluation procedures were performed using the Scikit-Learn v1.3.0 library, except for the XGBoost models, which used the XGBoost library, all implemented in Python v3.11.5 on the same workstation used for the FE simulations, described in "FE Models" section.

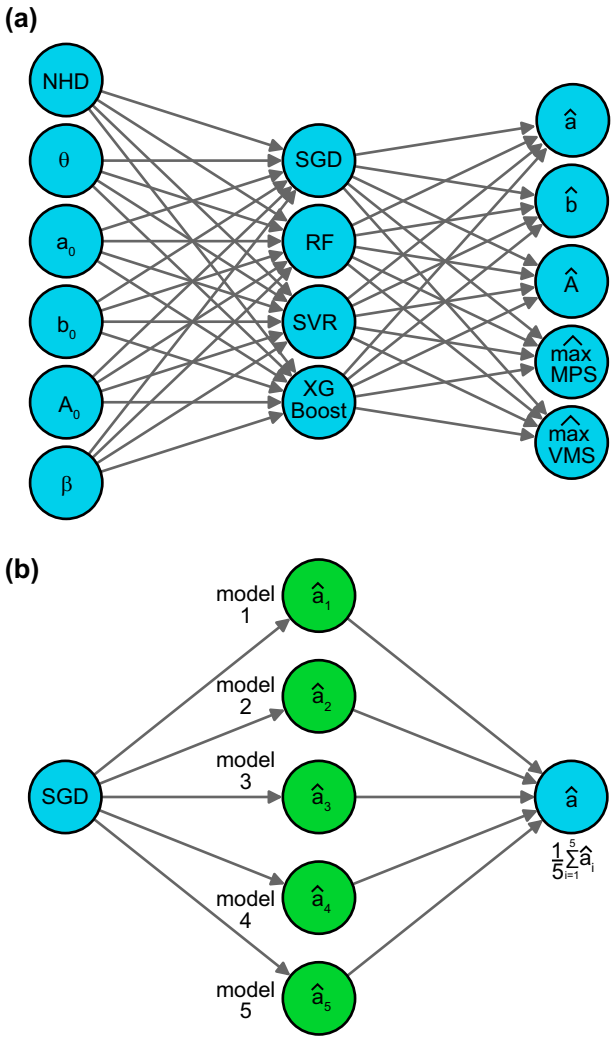

Fig. 2 Flowcharts illustrating: **a** the supervised learning framework, showing the input features (NHD, θ, a_0, b_0, A_0, β) used to train four ML models (SGD, RF, SVR, XGBoost) to predict five output variables [$\hat{a}$, $\hat{b}$, $\hat{A}$, $\widehat{\max}$(MPS), $\widehat{\max}$(VMS)], and **b** the fivefold cross-validation scheme illustrated for the SGD model, where the average of the five predicted values $\hat{a}$ formed the final output

ML Model Evaluation

As discussed in the previous section, for each ML algorithm, we trained five separate models, one for each output variable, using a fivefold cross-validation procedure. To evaluate model performance, we used the coefficient of determination, R^2, which quantifies how well the predicted outputs match the ground-truth values from the FE simulations. For each training and testing set (e.g., given a total of 732 samples, we used $n = 586$ for training and $n = 146$ for testing), R^2 was computed as follows:

$$R^2 = 1 - \frac{\sum_{i=1}^{n}(y_i - \hat{y}_i)^2}{\sum_{i=1}^{n}(y_i - \bar{y})^2}, \tag{19}$$

where y_i is the FE output, $\hat{y}_i$ is the corresponding prediction from the ML model, and $\bar{y}$ is the mean of the FE values across all n samples in the respective set.

For evaluating model accuracy, we computed the R^2 score for both the training and testing sets in each cross-validation fold and averaged the results across the five folds. Since we trained 20 models corresponding to four algorithms applied to 5 output variables, this yielded 20 average training and 20 average testing R^2 scores. Higher R^2 values indicate better predictive accuracy, with a score of 1 denoting a perfect match between predicted and true values.

In addition to the R^2 score, model performance was also evaluated using the root MSE (RMSE), the square root of Eq. (18), which measures the average magnitude of prediction errors in the same physical units as the output variable. RMSE is particularly useful for assessing absolute predictive accuracy and penalizes larger errors more strongly than smaller ones. Similar to the R^2 analysis, RMSE values were calculated separately for the training and testing sets in each cross-validation fold and then averaged across the five folds. Lower RMSE values indicate better predictive performance, corresponding to smaller discrepancies between predicted and ground-truth FE values. Together, the R^2 and RMSE metrics provide complementary assessments of model performance by capturing both relative goodness-of-fit and absolute prediction error.

For each algorithm and output variable, we recorded the training time across the five cross-validation folds and reported the average as the mean training time. To evaluate predictive accuracy of the best-performing model, we generated scatter plots comparing predicted values to FE simulation results. Closeness to the identity line indicate the degree of agreement between predictions and ground truth. Finally, in order to quantify feature importance, we performed a permutation test by shuffling each input feature

10 times independently while holding other features constant. The resulting decrease in the model's R^2 score was used to estimate the relative contribution of each feature to model performance.

Results

FE Simulations

The HGO material parameters that yielded results consistent with the experimental data from swine vaginal tissue reported by McGuire et al. [10] are presented in Table 3. While efforts were made to maintain consistent parameters across the NT, LT, and CT configurations, adjustments to k_1, which relates to the stiffness of the fibers, and κ, which defines how disperse the fibers are, were necessary to improve agreement with experimental observations. Specifically, k_1 increased from 1400 kPa in the NT case to 3720 kPa and 4000 kPa in the LT and CT cases, respectively. Similarly, κ increased from 0.3000 in the NT case to 0.3325 in the LT case and 0.3200 in the CT case. The stress values at NHD = 1.05, 1.10, and 1.15 obtained with these parameters are shown in Fig. 3a. To provide an approximate measure of agreement, we calculated the normalized RMSE using FE predicted and experimental stress values at NHD levels of 1.05, 1.10, and 1.15. This error ranged from 0 to 14% across all NT, LT, and CT cases in both LD and CD, indicating good alignment with the experimental trends given the inherent variability in the data.

Figure 3b shows the stress versus NHD results from simulations of vaginal tissue with NT, LT, and CT geometries using the baseline material parameters reported in Table 3, which are the parameters computed by fitting data from the NT group. These simulations were conducted to isolate and examine the mechanical effects of the tears alone, that is the difference in the NT, LT, and CT geometries. As expected, axial stresses were higher at each NHD in the LD compared to the CD for all configurations, consistent with the alignment of the mean preferred fiber direction along the LD. The overall stress magnitudes in the LD decreased progressively from NT to LT to CT. This trend is due to the weakening

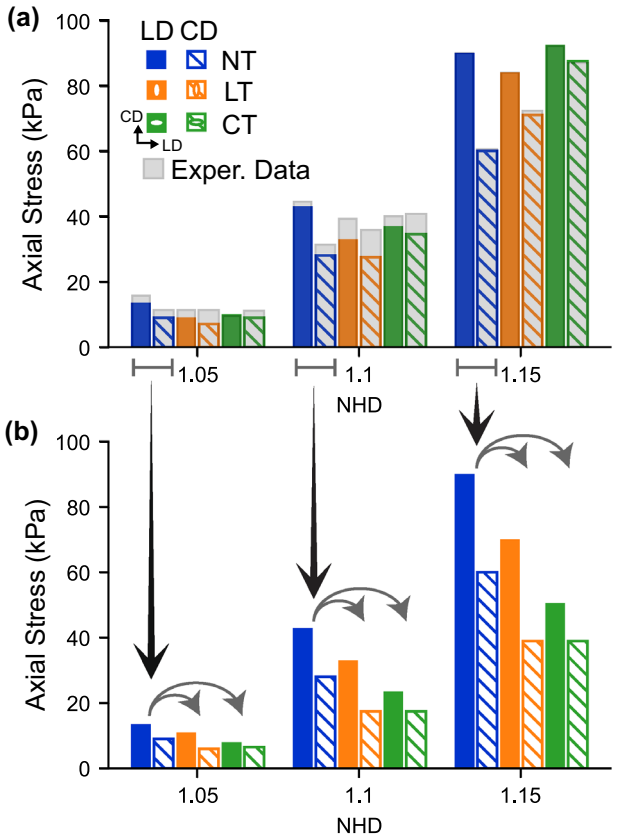

Fig. 3 Axial stress values, obtained from reaction forces at hooks divided by the cross-sectional area along the LD and CD, at NHD = 1.05, 1.10, and 1.15 for the NT, LT, and CT geometries **a** using different sets of material parameters for each geometry, as reported in Table 3, to reproduce average experimental results by McGuire et al. [10] (in gray), and **b** using fixed baseline material parameters reported in Table 3

effect of tears, particularly when oriented perpendicular to the dominant fiber direction, as in the CT case. The stress magnitude in the CD was higher for the NT configuration than for the LT and CT cases at each NHD, while the stresses for LT and CT remained nearly identical across all NHD values. The similar stress magnitudes observed in the CD, for both LT and CT configurations, demonstrate that when fibers were predominantly aligned in the LD, the stress at the hooks, away from the tear, became largely independent

Table 3 Material parameters in the HGO constitutive model [Eqs. (1)–(2)] identified by running FE simulations and adjusting values to best match the experimental stress–NHD data for NT, LT, and CT configurations reported by McGuire et al. [10], while keeping parameters as consistent as possible across configurations

Case	c (kPa)	D (kPa)	k_1 (kPa)	k_2	α	β (°)	κ
NT (Baseline)	10	6.7	1400	1	1	0	0.30
LT ($\theta = 0°$)	10	6.7	3720	1	1	0	0.33
CT ($\theta = 90°$)	10	6.7	4000	1	1	0	0.32

of tear orientation. Since the fibers contributed minimally to resisting loading in the CD, a tear in either direction disrupted the load transfer in a comparable manner. In other words, the stress in the CD was mainly governed by the non-fibrous matrix [i.e., the first term in Eq. (1)] so any tear weakened the tissue in a similar way in the CD, regardless of its orientation. To further analyze the impact of tear orientation, we varied the angle, θ, between the semi-major axis of the tear and the LD in the FE simulations, still keeping the tear size and HGO material parameters fixed to the baseline values (Tables 1, 3).

The results of FE simulations of vaginal tissue specimens in the NT, LT, and CT configurations are shown in Fig. 4. As anticipated, introducing a tear led to localized displacement at the tear site, whereas the NT specimen exhibited smaller displacements at the center due to symmetry and applied boundary conditions. Figure 5 presents the simulation results for additional tear angles of $\theta = 22.5°, 45°, 67.5°$, for NHD values of 1.00, 1.05, 1.10, 1.15. As the tear became more aligned with the CD (i.e., going from 22.5° to 67.5°), the local displacement around the tear increased, indicating a greater mechanical disruption in that region.

To further investigate tear behavior, we extracted the max MPS and VMS values from each simulation as we varied tear orientations, tear sizes, and mean preferred fiber orientations at each NHD. Figure 6a presents the MPS and VMS across the entire geometry for one case, the LT geometry, with baseline tear size and baseline material parameters reported in Tables 1 and 3, respectively, while Fig. 6b provides a zoomed-in view of the region around the tear in Fig. 6a, indicating where max MPS and VMS were recorded. As shown in Fig. 7a, the max VMS monotonically increased as the semi-major axis of the tear became more aligned with the CD direction. Specifically, the max VMS rose from 242 kPa at 0° to 383 kPa and 552 kPa at 22.5° and 45°, respectively. However, beyond 45°, the increase was less pronounced, reaching 567 kPa at 67.5° and 577 kPa at 90°. These results indicate a sharp increase in max VMS as the tear orientation shifted from 0° to 45°, beyond which the max VMS leveled off with only minor increases up to 90°. The max MPS changed non-monotonically as the tear angle increased from 0° (aligned with the LD) to 90° (aligned with the CD). This strain quantity, which was 0.43 at 0°, increased by 0.02 at 22.5° and by another 0.01 to reach a peak of 0.46 at 45°. It then decreased by 0.03 from 45° to 67.5°, and by 0.04 from 67.5° to 90°, resulting in a final value of 0.40 at NHD = 1.15.

The semi-major and semi-minor axes of the elliptical tear were varied in the LT configuration to evaluate how tear size affects the mechanical response of vaginal tissue. The selected values of these axes were chosen in the same range as the values reported by McGuire et al. [10]. Simulation results are shown in Fig. 8, where larger tears due to larger a_0 or b_0 caused more displacement in the CD as the tissue freely displaced in that direction. Figure 7b shows the max MPS and VMS around the tear versus NHD for different tear sizes. As depicted in Fig. 7b, varying the tear size by changing the semi-major axis a_0 resulted in comparatively modest changes in the mechanical response near the tear, with max MPS and VMS curves remaining close to those of the baseline configuration. In contrast, changes in the semi-minor axis b_0 had a pronounced effect on the local mechanics. Increasing b_0 led to a reduction in both max VMS and MPS; at NHD = 1.15, max VMS decreased from 242 to 189 kPa (approximately 22%), while max MPS decreased from 0.43 to 0.40. Conversely, decreasing b_0 amplified the mechanical response, with max VMS and MPS at NHD = 1.15 increasing to 300 kPa (approximately 24%) and 0.46, respectively. These results indicate that tear widening along the minor axis strongly modulates local stress and strain concentrations, whereas elongation along the major axis plays a comparatively secondary role.

Finally, we studied how varying the mean preferred fiber orientation influenced vaginal tissue behavior in the LT geometry. In this case, we considered two fiber families, with their orientations defined by the unit vectors $\boldsymbol{a}_1 = (0, \cos(\beta), \sin(\beta))$ and $\boldsymbol{a}_2 = (0, \cos(-\beta), \sin(-\beta))$, representing fibers symmetrically aligned at angles β and $-\beta$ with respect to the LD. Figure 9 shows the displacement magnitude predicted by the FE simulations at NHD values of 1.05, 1.10, and 1.15 for $\beta = 15°, 30°$, and 45°. As the fibers became increasingly misaligned with the LD, the tissue offered less resistance along that direction, allowing the tear to displace more at its sides (along the minor axis). Figure 7c presents the resulting max VMS and MPS as functions of NHD, corresponding to different values of the mean preferred fiber orientation. As shown in Fig. 7c, increasing the mean preferred fiber orientation angle from 0° to 45° led to a gradual increase in max VMS, with the rise becoming more pronounced as the angle approached 45°. The max VMS at NHD = 1.15 increased from 242 kPa at 0° to 278 kPa, 322 kPa, and 392 kPa at 15°, 30°, and 45°, respectively. In contrast, increasing the mean preferred fiber orientation resulted in a gradual decrease in max MPS. Specifically, the max MPS at NHD = 1.15 decreased from 0.43 at 0° to 0.41 at 45°, corresponding to an approximately 5% reduction.

ML Models

The performance of four algorithms, SGD, RF, SVR, and XGBoost, was compared using the average cross-validated R^2 scores across five output variables, a, b, A, $\widehat{\max}$(MPS), and $\widehat{\max}$(VMS), for both training and testing datasets (Fig. 10). The training dataset results represent the average performance obtained from fivefold cross-validation (see, for one example, Fig. 2b). As illustrated in

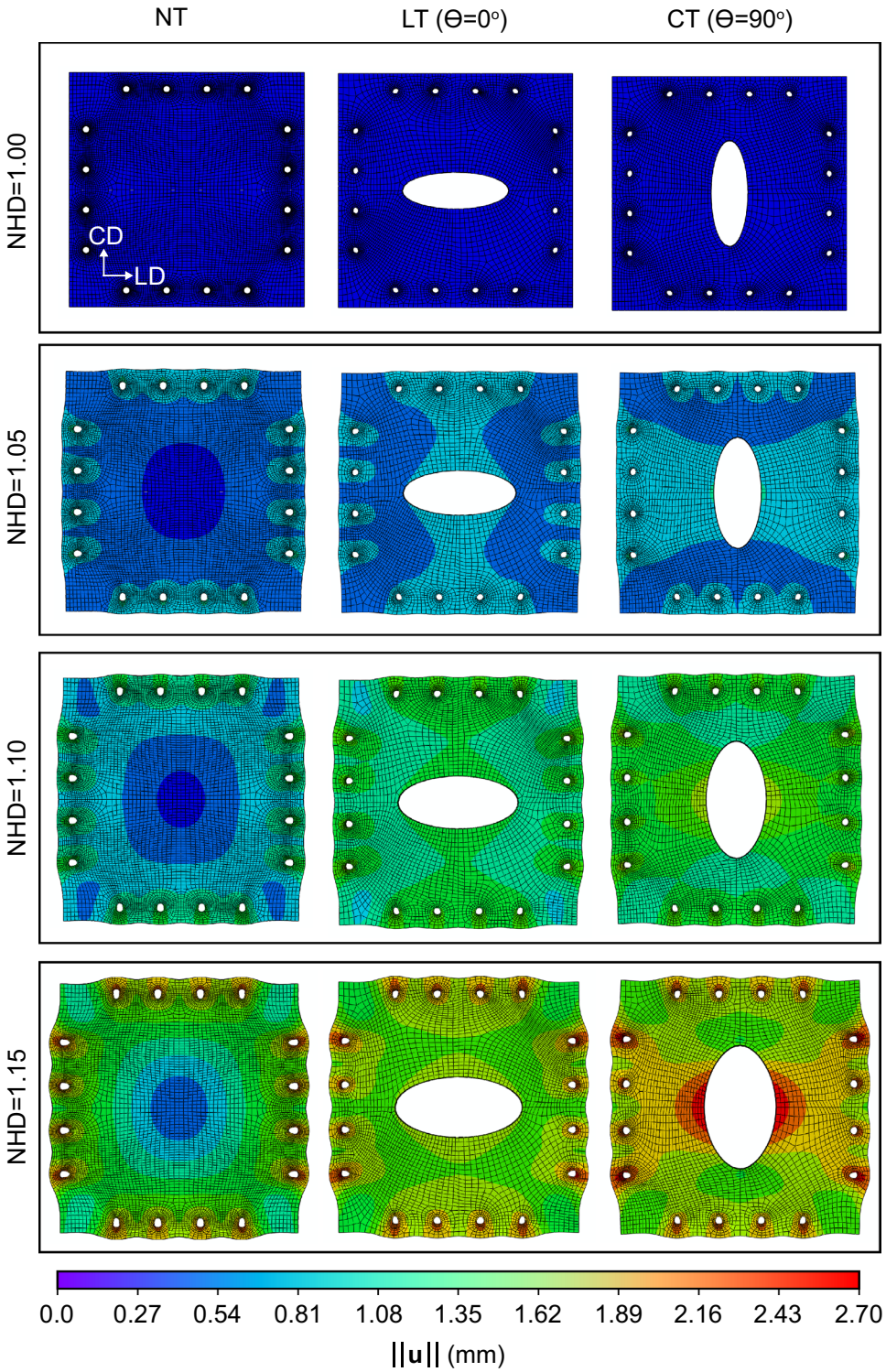

Fig. 4 Displacement vector magnitude for vaginal tissue with NT, LT ($\theta = 0°$), and CT ($\theta = 90°$) at NHD = 1.00 (undeformed configuration), 1.05, 1.10, and 1.15. Initial tear size and material parameters were fixed to baseline values (Tables 1, 3)

Fig. 10, the XGBoost model achieved the highest performance, with R^2 scores exceeding 0.99 across all outputs. The RF model ranked second, with results comparable to XGBoost, achieving R^2 scores above 0.97. In contrast, the linear regression with SGD and SVR algorithms showed relatively weaker predictive capabilities for max MPS and VMS (Fig. 10a). Nevertheless, linear regression with SGD considerably outperformed SVR in predicting max MPS, max VMS, and tear area during deformation, whereas SVR slightly outperformed linear regression with SGD in predicting the semi-minor and semi-major axes. The only

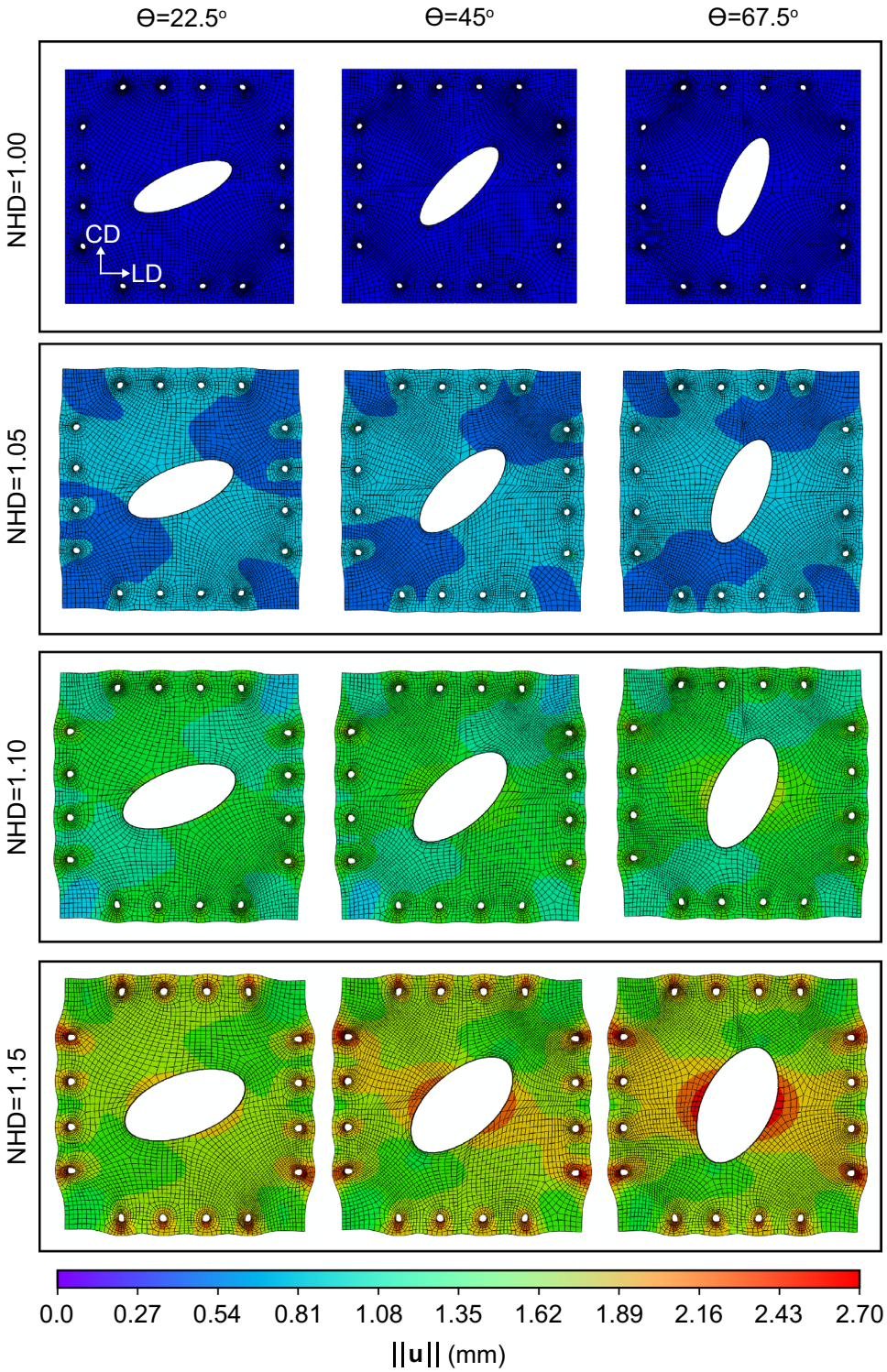

Fig. 5 Displacement vector magnitude for vaginal tissue with tear at $\theta = 22.5°$, 45°, and 67.5°, relative to the LD ($\theta = 0°$), at NHD = 1.00 (undeformed configuration), 1.05, 1.10, and 1.15. Initial tear size and material parameters were fixed to baseline values (Tables 1, 3)

cases where the R^2 score dropped below 0.75 occurred with the SVR in predicting max VMS (Fig. 10a).

A similar trend was observed in the R^2 scores for the testing dataset, as illustrated in Fig. 10b. XGBoost and RF emerged as the top-performing models for predicting unseen data, achieving R^2 scores 0.99 and 0.97, respectively, across all outputs. Both SGD and SVR performed well in predicting semi-minor and semi-major axes during

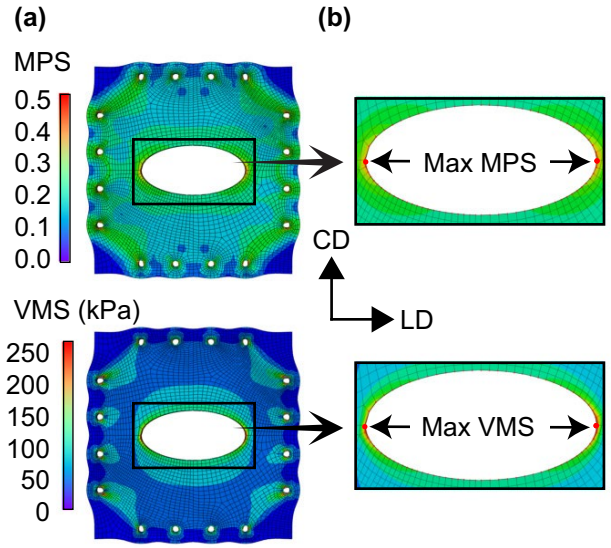

Fig. 6 Max MPS and VMS for the LT configuration at NHD = 1.15: **a** full geometry and **b** zoomed-in view near the tear. Red dots in **b** indicate the locations of max MPS and VMS for this specific model. Initial tear size and material parameters were fixed to baseline values (Tables 1, 3)

deformation, although linear regression with SGD demonstrated better predictive performance for max VMS, max MPS, and area. Additionally, the SVR model again recorded an R^2 score below 0.75 for max VMS prediction. The RMSE results, provided in the Supplementary Material (Supplementary Fig. 1), further confirm the comparable performance of the tree-based models, with the XGBoost model still performing better than the RF model, given its lower RMSE values.

Next, we compared the training times of the models to analyze the trade-offs between speed and performance. Table 4 reports the average training time required by each algorithm to build models for all outputs, calculated based on fivefold cross-validation. As described in "Methods" section, we first averaged the training time across the five cross-validation folds for each output and then summed these averages across all outputs for each algorithm. XGBoost required significantly more training time, averaging 10.5 s, approximately 20 times slower than RF. In contrast, SGD and SVR were much faster, with linear regression with SGD being the fastest at only 0.07 seconds on average, making it roughly 150 times faster than XGBoost.

Figure 11a–e presents a detailed comparison between the FE-generated values of max MPS, max VMS, a, b, A, and the corresponding predictions made by XGBoost. The trained models accurately predict strain and stress values around the tear, as well as the semi-minor axis, semi-major axis, and tear area during deformation for unseen data (Fig. 11a–e). Ideal predictions would lie exactly on

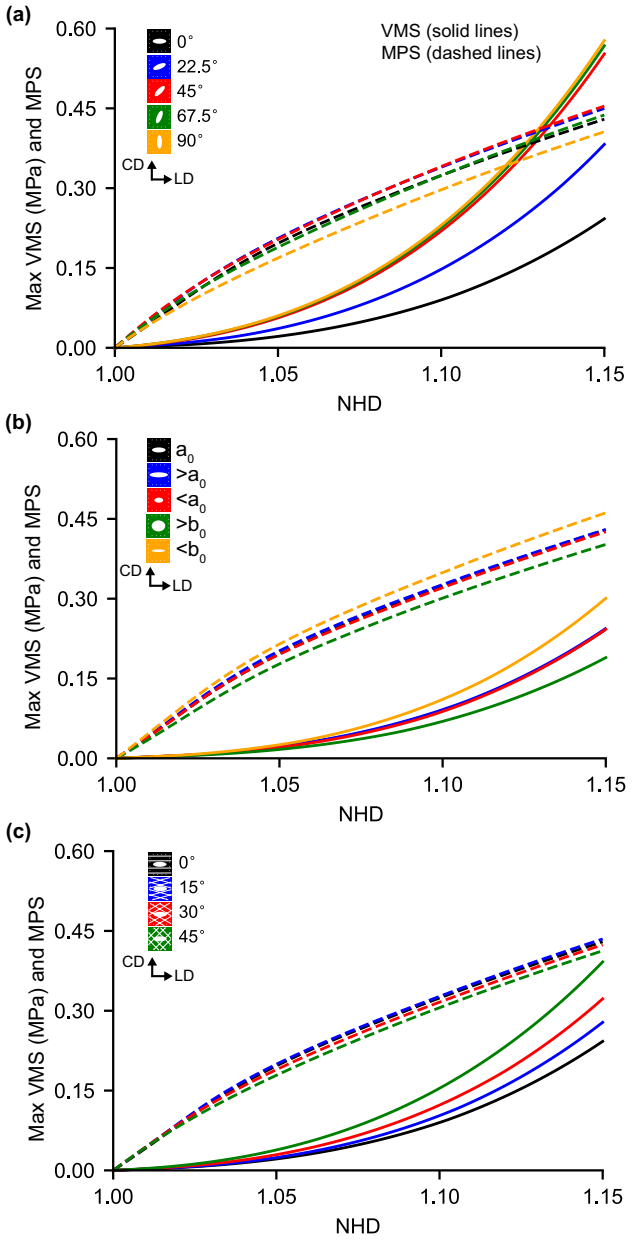

Fig. 7 Max VMS and MPS versus NHD around the tear. **a** Tears of fixed size (baseline size reported in Table 1) with orientations ranging from $\theta = 0°$ (LT) to $\theta = 90°$ (CT) in 22.5° increments. **b** Tears aligned in the LD of different sizes, defined by semi-major axis, a_0, and semi-minor axis, b_0, reported in Table 1. Black lines lie beneath the blue lines. **c** Mean preferred fiber orientations defined by $\pm\beta$ ranging from 0° to 45° in 15° increments. Tears of fixed size (baseline size reported in Table 1) were aligned in the LD. Simulations in **a**–**c** were performed using baseline material parameters reported in Table 3. However, in **c**, two families of fibers ($\alpha = 2$) were selected, with $k_1 = 700$ kPa for each family

the identity line, indicating perfect agreement between FE-generated and ML-predicted data; deviations from this line represent prediction error. As observed in Fig. 11a–e, nearly all points lie on or are very close to the identity line across

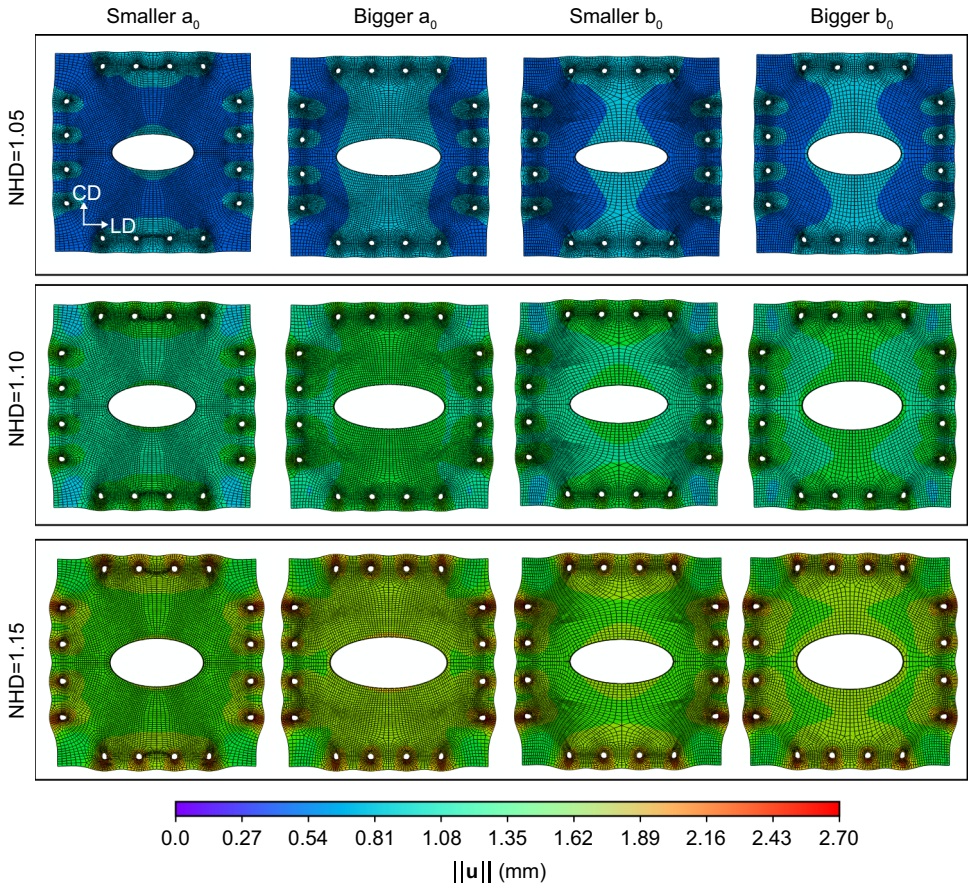

Fig. 8 Displacement vector magnitude for vaginal tissue with LT geometry at NHD = 1.05, 1.10, and 1.15. Initial tear size varied as specified in Table 1, and material parameters were fixed to baseline values (Table 3)

all outputs, demonstrating the robustness and predictive accuracy of the trained models.

A permutation test was employed to quantify the contribution of each input feature in the XGBoost models. Figure 11f–j illustrates the mean drop in R^2 score caused by independently shuffling each input feature and measuring its impact on the predictive performance of the models. The NHD feature was excluded from this test due to its fundamental role across all outputs, as predictions were inherently made over varying NHD values as the tear developed. Figure 11g, i shows that the initial tear orientation was the most influential feature in predicting max VMS and semi-minor axis b during extension. Specifically, tear orientation significantly impacted max VMS prediction, resulting in an R^2 drop of approximately 0.44. It was also the second-most influential feature for predicting max MPS and tear area. For the semi-major axis a prediction during deformation, its initial value had the largest influence, decreasing the R^2 score by approximately 0.26 when permuted (Fig. 11h). For max MPS prediction, the initial semi-minor axis b_0 and tear orientation showed some influence; however, their respective drops in R^2 scores were relatively small (Fig. 11f). This suggests that no single parameter dominated max MPS prediction significantly, and all parameters collectively contributed to prediction accuracy. Nonetheless, tear orientation θ and initial semi-minor axis b_0 remained critical for accurately predicting max VMS and semi-minor axis b, due to their high importance scores. Similar results to those reported in Fig. 11 for the SGD, RF, and SVR models are presented in Supplementary Figs. 2, 3, and 4 in Supplementary Material.

Discussion

In this study, we developed a series of FE models to investigate how tears affect the mechanical behavior of vaginal tissue, as demonstrated through ex vivo planar biaxial testing of swine vaginal tissue [34]. We conducted simulations in which we systematically varied tear orientation, tear size, and tissue anisotropy to evaluate their individual effects on tissue mechanics. This modeling approach complemented the experimental studies and provided synthetic data that are otherwise challenging, resource-intensive, and limited in their ability to isolate the contributions of specific mechanical factors. Building on the FE results, we trained ML models to rapidly predict mechanical responses and tear characteristics across a range of predefined fiber orientations and tear geometries.

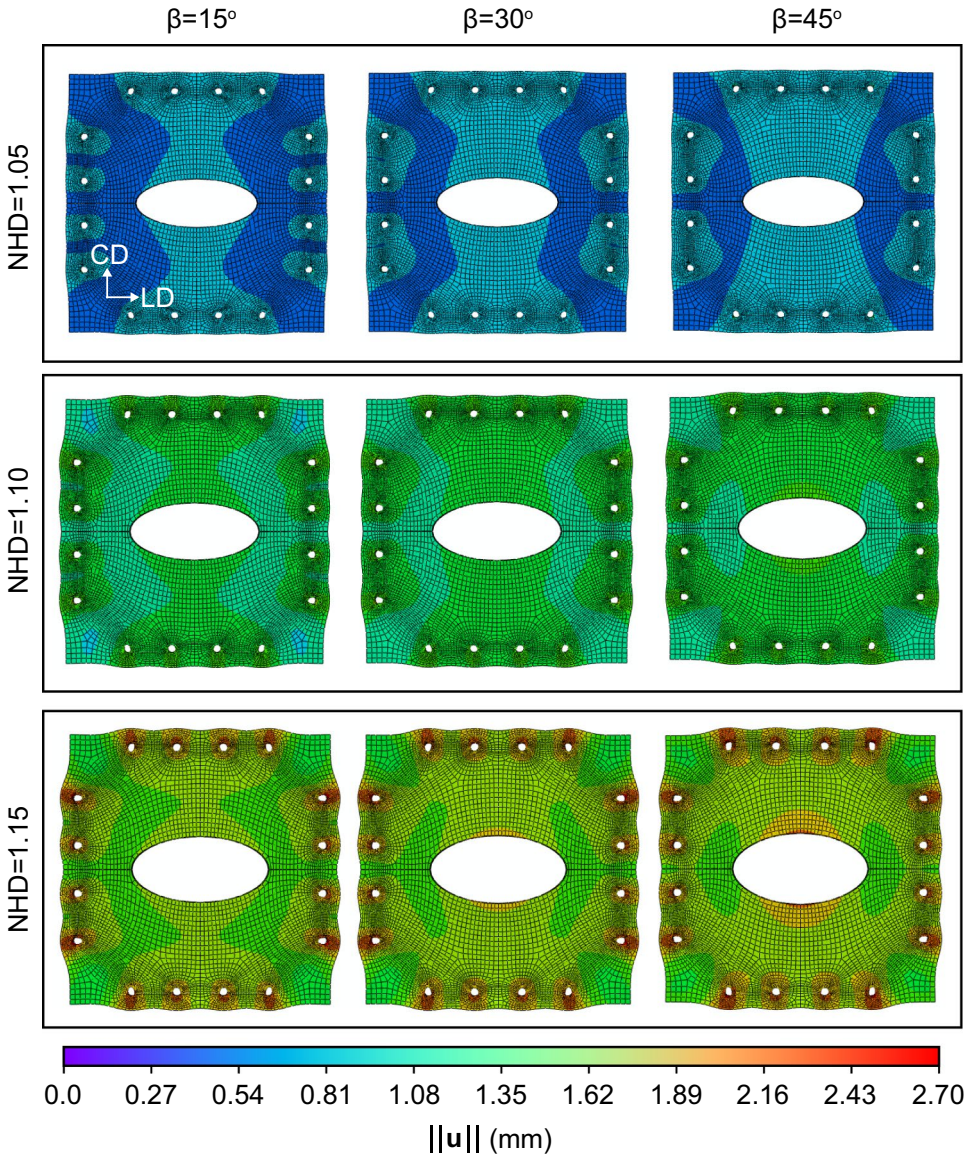

Fig. 9 Displacement vector magnitude for vaginal tissue with LT geometry at NHD = 1.05, 1.10, and 1.15. Initial tear size was fixed to baseline values (Table 1) and material parameters were fixed to baseline values (Table 3), except for $\alpha = 2$ and $k_1 = 700$ kPa

FE Model Calibration

The first step of this study consisted in selecting the appropriate values for the HGO constitutive model to reproduce experimental observations from swine vaginal tissue [10]. Toward this end, we calibrated the model using initial parameter estimates followed by iterative refinement until satisfactory agreement with the experimental results for specimens from the NT, LT, and CT groups was achieved, within the variability observed in the data (Fig. 3a). Although the same material model was applied to NT, LT, and CT specimens, we found that a single set of material parameters could not reproduce the average mechanical response in all cases. Specifically, the FE models of torn specimens required a higher k_1 value to match the experimental data. This discrepancy arises because, while the overall geometry was consistent across experimental and FE models, the representation of the tear differs between experiments and simulations. In the experiments, a line cut was introduced into an intact specimen, preserving the total tissue volume; upon loading, this cut immediately opened and evolved into an approximately elliptical shape through deformation and fiber redistribution, without removal of material. In contrast, the FE model excluded the torn region entirely by prescribing an elliptical void in the geometry, thereby removing material volume a priori, altering stress paths and stiffness distribution. We also increased the dispersion parameter, κ, in specimens with tears (Table 3). Although κ is relatively high even in the baseline (NT) case, this reflects the largely isotropic macroscopic response observed over the

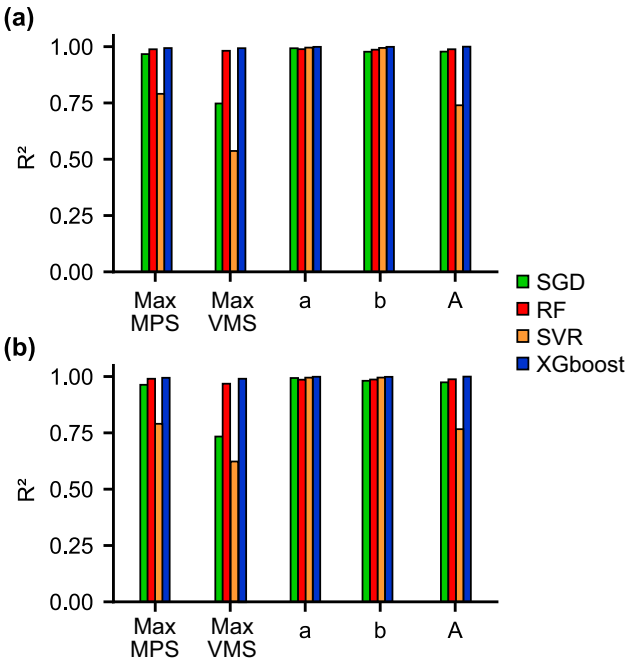

Fig. 10 Comparison of average cross-validated R^2 scores for **a** training and **b** testing datasets, obtained from predicting max MPS, max VMS, semi-major axis a, semi-minor axis b, and tear area A during deformation, using SGD, SVR, RF, and XGBoost

Table 4 Average training time required by each ML algorithm to train all outputs, computed using fivefold cross-validation

ML algorithm	Average training time (s)
SGD	0.07
RF	0.53
SVR	0.09
XGBoost	10.5

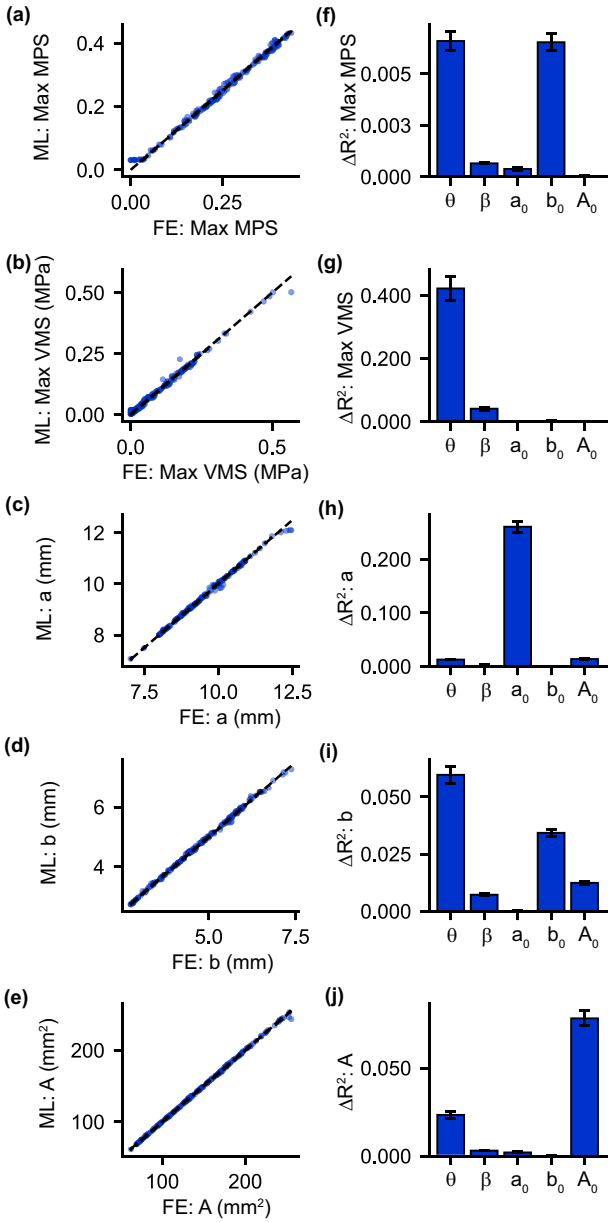

Fig. 11 **a**–**e** Comparison between FE-generated data and XGBoost model predictions for **a** max MPS, **b** max VMS, **c** semi-major axis a, **d** semi-minor axis b, and **e** tear area A during deformation. The black dashed line represents the ideal case in which predicted values exactly match the FE-generated data. **f**–**j** Bar plots showing the drop in R^2, ΔR^2, when each input feature, θ, β, a_0, b_0, A_0, was permuted in the XGBoost models predicting **f** max MPS, **g** max VMS, **h** semi-major axis a, **i** semi-minor axis b, and **j** tear area A during deformation. Whiskers denote standard deviation across 10 repetitions

strain range examined, with pronounced anisotropy likely emerging at higher stretches. Consequently, fiber contributions appear weak because the applied deformations do not strongly recruit or align collagen fibers. While fibers may locally reorient near tear tips to resist further opening, such highly localized effects cannot be represented within the homogeneous HGO framework. Therefore, variations in κ should be interpreted as an effective, spatially averaged representation of heterogeneous local fiber kinematics rather than as damage-induced remodeling or increased isotropy.

Effects of Tear Orientation and Size

The displacement magnitude maps in Figs. 4 and 5 show increased displacement concentrated around the co-vertices of the elliptical tear when the tear orientations are misaligned with the LD. The observed behavior can be attributed to a reduction in load-bearing capacity along the LD as the tear orientation angle θ increased from 0° to 90°, assuming the fibers were predominantly aligned along the LD. These findings are consistent with those of McGuire

et al. [10], who reported that tear area increased more significantly with NHD in the CT group compared to the LT group. Additionally, our simulations demonstrated that when the tear was aligned with the LD, max MPS was lowest, reflecting the increased local stiffness provided by fiber alignment in that direction (Fig. 7a). As the tear rotated away from the mean fiber direction, this structural reinforcement diminished along the tear's major axis, allowing for greater local deformation and elevated MPS. Notably, both MPS and VMS peaked at approximately 45°, where the tear orientation was oblique to both principal directions, thereby maximizing local stress concentrations. Beyond 45°, as the tear approached alignment with the CD, max MPS slightly decreased while max VMS continued to rise (Fig. 7a).

Not surprisingly, tears of bigger size caused larger displacement within the tissue around the tear (Fig. 8). Figure 7b illustrates that max VMS decreased at higher NHDs as the initial semi-minor axis b_0 of the tear increased. This reduction can be explained by the removal of portions of the geometry containing collagen fibers aligned with the LD. Conversely, when the semi-minor axis was smaller, the geometry of the vaginal tissue had more collagen fibers in the LD, which provided greater resistance and led to higher VMS around the tear. A similar trend is observed for max MPS in Fig. 7b, where increases in VMS were accompanied by increases in MPS. On the other hand, changing the tear size by varying the initial semi-major axis a_0 had little effect on the stress or strain distribution around the tear. This is because these variations did not significantly alter the tissue's geometry along the LD, the primary orientation of fibers.

Role of Fiber Orientation

Because fiber orientation in vaginal tissue from swine and other animal models has not been quantified, in our FE simulations, we altered the constitutive parameter β that defined the mean preferred directions of two symmetric fiber families. With the tear oriented in the LD, when the mean preferred fiber directions deviated from the LD, the magnitude of the displacement increased at the side of the tear (Fig. 9). This led to a steady rise in max VMS and a corresponding decrease in max MPS (Fig. 7c), suggesting that, when the tear was aligned with the dominant fiber directions, stress around the tear was minimized under identical stretch conditions. The fiber alignment in the LD reduced stress concentrations at the tear edges because the continuous fiber network distributes the load more evenly, preventing localized stress buildup. Our findings indicate that considering fiber orientation in episiotomies, where an incision is made in the perineal region/posterior vagina to enlarge the vaginal opening during childbirth, may lower stress and limit tear extension. Specifically, aligning the incision with the dominant collagen fiber orientation may reduce stress concentrations and tear propagation by preserving continuous load transfer along collagen fibers, thereby promoting controlled healing.

ML Model Comparison and Performance

To our knowledge, the only other application of integrated FE–ML approaches in pelvic floor biomechanics is the work by Moura et al. [32]. They developed an FE–ML framework to predict maximum stress in the pelvic floor muscle during childbirth, conducting FE simulations on a single anatomical geometry, generating synthetic datasets by varying constitutive model parameters, and training multiple ML models. Thus, while FE–ML frameworks have recently been explored in this field, our study differs in both anatomical focus and objective. We apply an FE–ML approach to vaginal tissue with pre-existing tears, using synthetic datasets generated by varying both anatomical geometry and material properties to predict tear behavior, a topic that remains understudied in biomechanics.

For the ML component of this study, we compared linear (SGD), kernel-based (SVR), and tree-based algorithms (RF and XGBoost) to characterize tear behavior in vaginal tissue (Fig. 10). By leveraging these well-established ML algorithms, we have established a strong foundation for modeling tear behavior. Future work incorporating advanced techniques such as deep learning and neural networks, which have already shown remarkable success in our recent tear propagation research [25] and the work of Moura et al. [32], offers exciting potential for even greater performance.

ML models trained within seconds (Table 4) and generated predictions in milliseconds, offering a practical alternative to computationally intensive FE simulations, which can require minutes to hours per case. Among the evaluated models, RF provided a favorable balance between accuracy and efficiency, achieving $R^2 = 0.97$ while training approximately 20 times faster than XGBoost. Although XGBoost achieved a marginally higher accuracy, the comparatively small performance reduction observed for RF suggests it may be a more practical choice for larger datasets or clinical workflows where rapid model training, frequent updates, or limited computational resources are important considerations.

ML Feature Importance

Our findings show that tear orientation is the most critical feature for predicting max VMS (Fig. 11g and Supplementary Figs. 2g, 3g, 4g for all ML models). This is consistent with previous FE analysis on episiotomy, which demonstrated that incision angles influence stress–strain behavior of the pelvic floor muscle, muscle tear propagation, and overall tear area [44]. The variations in the semi-major axis

and tear area during deformation were best predicted by their respective initial values, although for the semi-minor axis, tear orientation emerged as the primary determinant (Fig. 11h–j and Supplementary Figs. 2h–j, 3h–j, 4h–j for all models). This observation is consistent with Fig. 4, which shows that as tear orientation deviates from the LD, displacement around the semi-minor axis increases, resulting in a wider tear from the LT to the CT case.

Limitations and Future Directions

Our finite element simulations were intentionally simplified to isolate specific factors contributing to tear behavior. For this reason, we assumed that the vaginal tissue had uniform material properties, whereas the vaginal canal consists of four distinct histological layers and is anatomically divided into distal, mid, and proximal sections, each with likely differing mechanical properties [34, 45]. Consistent with this approach, we did not account for spatial variations in fiber orientation near and far from the tear [34]. The HGO formulation assumes a homogenized fiber distribution with fixed mean orientation. Consequently, the computed mechanical response near the tear reflects continuum-level stress–strain redistribution, while potential microscale toughening mechanisms associated with tear-tip fiber reorientation, such as blunting-induced deformation redistribution, are not explicitly resolved. This type of reorganization has been shown to resist tear propagation by dissipating stress [34, 46, 47]. Future studies should incorporate anatomical and structural variations, as well as time-dependent material behavior [11, 48], to improve the accuracy and predictive capability of FE models for vaginal tissue mechanics. However, experimental work is needed to fully characterize region- and layer-specific micromechanical properties, as well as the time-dependent behavior of vaginal tissue.

The main benefit of integrating FE simulations with ML models is their ability to predict tissue behavior for arbitrary input conditions, even in cases without prior simulations or experimental data. Despite this advantage, our approach is not without limitations. While FE simulations provide a controlled and cost-effective way to generate training data, they cannot fully capture the complexity of real tissue behavior. Experimental data, though free from the simplifying assumptions of FE modeling, are often expensive or difficult to obtain, as direct testing on vaginal tissue, particularly during pregnancy, is neither feasible nor permissible. Our dataset was also relatively small due to time and resource limitations, so this study served as a proof of concept focused on feasibility rather than optimal model performance. Despite these limitations, the models performed well, suggesting that integrating FE with experimental data, increasing dataset diversity, and leveraging advanced ML techniques could enhance accuracy and robustness, and facilitate multi-output predictions in a unified framework, with future extensions naturally incorporating variability in material parameters.

Clinical and Biomechanical Implications

Geometrical factors (e.g., initial tear size and shape) and material properties (e.g., anisotropy and fiber orientation) govern the mechanical behavior of vaginal tissue tears, which account for approximately 21% of birth-related injuries [49]. Although these tears often heal naturally *in vivo*, some can extend into deeper layers, reaching the pelvic muscles, perineum, or anal sphincter, and they require medical intervention. By quantifying stress and strain patterns around tears, predictive models can be refined to develop more effective approaches for preventing severe injuries, protecting important pelvic structures, and ultimately improving health outcomes for women before and after childbirth.

Supplementary Information The online version contains supplementary material available at https://doi.org/10.1007/s10439-026-04055-3.

Acknowledgments We acknowledge the support of the National Science Foundation (NSF) through Grant No. 2135683.

Author Contributions MZ contributed to the conceptualization, data curation, methodology, software development, investigation, formal analysis, validation, visualization, and both drafting and editing of the manuscript. JK contributed to the conceptualization, methodology, investigation, supervision, and manuscript review and editing. TI contributed to the conceptualization, methodology, investigation, supervision, and manuscript review and editing. RD contributed to the conceptualization, software development, visualization, supervision, project administration, resources, and both the original drafting and critical revision of the manuscript. All authors read and approved the final manuscript.

Funding This work was supported by NSF under Grant No. 2135683.

Data Availability The datasets generated during the current study are available from the corresponding author on reasonable request.Consent for Publication Not applicable.

Declarations

Conflict of interest The authors declare no conflict of interest.

Ethical Approval Not applicable.

Informed Consent Not applicable.

Clinical Trial Number Not applicable.

References

1. Samuelsson, E., L. Ladfors, B. Lindblom, and H. Hagberg. A prospective observational study on tears during vaginal delivery: occurrences and risk factors. *Acta Obstet. Gynecol. Scand.* 81(1):44–49, 2002.
2. Thranov, I., A. M. Kringelbach, E. Melchior, O. Olsen, and M. T. Damsgaard. Postpartum symptoms: episiotomy or tear at vaginal delivery. *Acta Obstet. Gynecol. Scand.* 69(1):11–15, 1990.
3. Jansson, M. H., K. Franzén, A. Hiyoshi, G. Tegerstedt, H. Dahlgren, and K. Nilsson. Risk factors for perineal and vaginal tears in primiparous women—the prospective POPRACT-cohort study. *BMC Pregnancy Childbirth*. 20:1–14, 2020.
4. Padoa, A., N. Glick Fishman, A. Tsviban, and N. Smorgick. Vaginal postcoital injuries requiring surgical intervention: a case series and literature review. *Int. J. Impot. Res.* 33(1):110–117, 2021.
5. Gabriel, N. M., M. Clayton, and S. P. Starling. Vaginal laceration as a result of blunt vehicular trauma. *J. Pediatr. Adolesc. Gynecol.* 22(5):e166–e168, 2009.
6. Strohbehn, K. Normal pelvic floor anatomy. *Obstet. Gynecol. Clin. N. Am.* 25(4):683–705, 1998.
7. Dubik, J., M. Alperin, and R. De Vita. The biomechanics of the vagina: a complete review of incomplete data. *NPJ Womens Health*. 3(1):4, 2025.
8. Peña, E., B. Calvo, M. Martínez, P. Martins, T. Mascarenhas, R. N. Jorge, et al. Experimental study and constitutive modeling of the viscoelastic mechanical properties of the human prolapsed vaginal tissue. *Biomech. Model. Mechanobiol.* 9(1):35–44, 2010.
9. Peña, E., P. Martins, T. Mascarenhas, R. N. Jorge, A. Ferreira, M. Doblaré, et al. Mechanical characterization of the softening behavior of human vaginal tissue. *J. Mech. Behav. Biomed. Mater.* 4(3):275–283, 2011.
10. McGuire, J. A., S. D. Abramowitch, S. Maiti, and R. De Vita. Swine vagina under planar biaxial loads: an investigation of large deformations and tears. *J. Biomech. Eng.* 141(4):041003, 2019.
11. Pack, E., J. Dubik, W. Snyder, A. Simon, S. Clark, and R. De Vita. Biaxial stress relaxation of vaginal tissue in pubertal gilts. *J. Biomech. Eng.* 142(3):031002, 2020.
12. Huntington, A., E. Rizzuto, S. Abramowitch, Z. Del Prete, and R. De Vita. Anisotropy of the passive and active rat vagina under biaxial loading. *Ann. Biomed. Eng.* 47(1):272–281, 2019.
13. Huntington, A., S. D. Abramowitch, P. A. Moalli, and R. De Vita. Strains induced in the vagina by smooth muscle contractions. *Acta Biomater.* 129:178–187, 2021.
14. Chanda, A., V. Unnikrishnan, S. Roy, and H. E. Richter. Computational modeling of the female pelvic support structures and organs to understand the mechanism of pelvic organ prolapse: a review. *Appl. Mech. Rev.* 67(4):040801, 2015.
15. Silva, M., S. Brandão, M. Parente, T. Mascarenhas, and J. R. Natal. Biomechanical properties of the pelvic floor muscles of continent and incontinent women using an inverse finite element analysis. *Comput. Methods Biomech. Biomed. Eng.* 20(8):842–852, 2017.
16. Grimm, M. J. Forces involved with labor and delivery—a biomechanical perspective. *Ann. Biomed. Eng.* 49(8):1819–1835, 2021.
17. Lien, K. C., B. Mooney, J. O. DeLancey, and J. A. Ashton-Miller. Levator ani muscle stretch induced by simulated vaginal birth. *Obstet. Gynecol.* 103(1):31–40, 2004.
18. Martins, J., M. Pato, E. Pires, R. N. Jorge, M. Parente, and T. Mascarenhas. Finite element studies of the deformation of the pelvic floor. *Ann. N. Y. Acad. Sci.* 1101(1):316–334, 2007.
19. Krofta, L., L. Havelková, I. Urbánková, M. Krčmář, L. Hynčík, and J. Feyereisl. Finite element model focused on stress distribution in the levator ani muscle during vaginal delivery. *Int. Urogynecol. J.* 28:275–284, 2017.
20. Lepage, J., C. Jayyosi, P. Lecomte-Grosbras, M. Brieu, C. Duriez, M. Cosson, et al. Biomechanical pregnant pelvic system model and numerical simulation of childbirth: impact of delivery on the uterosacral ligaments, preliminary results. *Int. Urogynecol. J.* 26(4):497–504, 2015.
21. Routzong, M. R., P. A. Moalli, S. Maiti, R. De Vita, and S. D. Abramowitch. Novel simulations to determine the impact of superficial perineal structures on vaginal delivery. *Interface Focus*. 9(4):20190011, 2019.
22. Asiedu, M. N., J. Agudogo, M. S. Krieger, R. Miros, R. J. Proeschold-Bell, J. W. Schmitt, et al. Design and preliminary analysis of a vaginal inserter for speculum-free cervical cancer screening. *PLoS ONE*. 12(5):e0177782, 2017.
23. Snyder, W., A. S. Anaya, J. Krometis, T. Iliescu, and R. De Vita. A numerical comparison of simplified Galerkin and machine learning reduced order models for vaginal deformations. *Comput. Math. Appl.* 152:168–180, 2023.
24. Snyder, W., J. A. McGuire, C. Mou, D. A. Dillard, T. Iliescu, and R. De Vita. Data-driven variational multiscale reduced order modeling of vaginal tissue inflation. *Int. J. Numer. Methods Biomed. Eng.* 39(1):e3660, 2023.
25. Snyder, W., M. Zakeri, J. Krometis, R. Batra, T. Iliescu, and R. De Vita. Deep learning reduced order models of vaginal tear propagation. *J. Mech. Behav. Biomed. Mater.* 170:107074, 2025.
26. Freutel, M., H. Schmidt, L. Dürselen, A. Ignatius, and F. Galbusera. Finite element modeling of soft tissues: material models, tissue interaction and challenges. *Clin. Biomech.* 29(4):363–372, 2014.
27. Phellan, R., B. Hachem, J. Clin, J. M. Mac-Thiong, and L. Duong. Real-time biomechanics using the finite element method and machine learning: review and perspective. *Med. Phys.* 48(1):7–18, 2021.
28. Li, C., S. Yang, H. Zheng, Y. Zhang, L. Wu, W. Xue, et al. Integration of machine learning with finite element analysis in materials science: a review. *J. Mater. Sci.* 60:8285–8307, 2025.
29. Akazawa, M., K. Hashimoto, N. Katsuhiko, and Y. Kaname. Machine learning approach for the prediction of postpartum hemorrhage in vaginal birth. *Sci. Rep.* 11(1):22620, 2021.
30. Park, S., J. Moon, N. Kang, Y. H. Kim, Y. A. You, E. Kwon, et al. Predicting preterm birth through vaginal microbiota, cervical length, and WBC using a machine learning model. *Front. Microbiol.* 13:912853, 2022.
31. Lipschuetz, M., J. Guedalia, A. Rottenstreich, M. N. Persky, S. M. Cohen, D. Kabiri, et al. Prediction of vaginal birth after cesarean deliveries using machine learning. *Am. J. Obstet. Gynecol.* 222(6):613-e1, 2020.
32. Moura, R., D. A. Oliveira, J. P. S. Ferreira, M. P. L. Parente, N. Kimmich, and R. M. Natal Jorge. A finite element-based machine learning framework to predict the mechanical behavior of the pelvic floor muscles during childbirth. *Expert Syst. Appl.* 250:123953, 2024.
33. Moura, R., D. A. Oliveira, M. P. Parente, N. Kimmich, L. Hynčík, L. H. Hympánová, et al. Patient-specific surrogate model to predict pelvic floor dynamics during vaginal delivery. *J. Mech. Behav. Biomed. Mater.* 160:106736, 2024.
34. McGuire, J. A., J. L. Monclova, A. C. S. Coariti, C. A. Stine, K. C. Toussaint Jr., J. M. Munson, et al. Tear propagation in vaginal tissue under inflation. *Acta Biomater.* 127:193–204, 2021.
35. Gruber, D. D., W. B. Warner, E. D. Lombardini, C. M. Zahn, and J. L. Buller. Anatomical and histological examination of the porcine vagina and supportive structures: in search of an ideal model for pelvic floor disorder evaluation and management. *Urogynecology*. 17(3):110–114, 2011.

36. Gasser, T. C., R. W. Ogden, and G. A. Holzapfel. Hyperelastic modelling of arterial layers with distributed collagen fibre orientations. *J. R. Soc. Interface*. 3(6):15–35, 2006.
37. McGuire, J. A., C. L. Crandall, S. D. Abramowitch, and R. De Vita. Inflation and rupture of vaginal tissue. *Interface Focus*. 9(4):20190029, 2019.
38. Bottou, L. Large-scale machine learning with stochastic gradient descent. In: Proceedings of the 19th International Conference on Computational Statistics (COMPSTAT), 2010. Springer, 2010, pp. 177–186.
39. Breiman, L. Random forests. *Mach. Learn.* 45:5–32, 2001.
40. Segal, M. R. Machine learning benchmarks and random forest regression. *Mach. Learn.* 54(1):5–32, 2004.
41. Hearst, M. A., S. T. Dumais, E. Osuna, J. Platt, and B. Scholkopf. Support vector machines. *IEEE Intell. Syst.* 13(4):18–28, 1998.
42. Ghorbani, M. A., H. A. Zadeh, M. Isazadeh, and O. Terzi. A comparative study of artificial neural network (MLP, RBF) and support vector machine models for river flow prediction. *Environ. Earth Sci.* 75:1–14, 2016.
43. Chen, T., and C. Guestrin. XGBoost: a scalable tree boosting system. In: Proceedings of the 22nd ACM SIGKDD International Conference on Knowledge Discovery and Data Mining, 2010. ACM, 2016, pp. 785–794.
44. Oliveira, D. A., M. P. Parente, B. Calvo, T. Mascarenhas, and R. M. N. Jorge. A biomechanical analysis on the impact of episiotomy during childbirth. *Biomech. Model. Mechanobiol.* 15:1523–1534, 2016.
45. Huntington, A. J., B. Udayasuryan, P. Du, S. S. Verbridge, S. D. Abramowitch, and R. D. Vita. Smooth muscle organization and nerves in the rat vagina: a first look using tissue clearing and immunolabeling. *Ann. Biomed. Eng.* 50(4):440–451, 2022.
46. Yang, W., V. R. Sherman, B. Gludovatz, E. Schaible, P. Stewart, R. O. Ritchie, et al. On the tear resistance of skin. *Nat. Commun.* 6(1):6649, 2015.
47. Bircher, K., M. Zündel, M. Pensalfini, A. E. Ehret, and E. Mazza. Tear resistance of soft collagenous tissues. *Nat. Commun.* 10(1):792, 2019.
48. Dubik, J., A. Tartaglione, K. Miller, D. Dillard, and R. De Vita. History-dependent deformations of rat vaginas under inflation. *Integr. Comp. Biol.* 62:625–640, 2022.
49. Hopkins, L. M., A. B. Caughey, D. V. Glidden, and R. K. Laros Jr. Racial/ethnic differences in perineal, vaginal and cervical lacerations. *Am. J. Obstet. Gynecol.* 193(2):455–459, 2005.